Physics-informed neural network for inverse modeling of natural-state geothermal systems

Kazuya Ishitsuka [*], Weiren Lin

Kyoto University, Nishikyo-ku, Kyoto, Japan

HIGHLIGHTS

- A physics-informed neural net (PINN) for geothermics is proposed for the first time.
- PINN predicts temperatures, pressures, and permeabilities in hydrothermal systems.
- PINN outperformed conventional neural networks in terms of prediction accuracy.
- PINN enhances physical validity of the predictions by considering conservation laws.
- PINN is useful for geothermal inverse modeling by combining data and physics laws.

ARTICLE INFO

ABSTRACT

Predicting the temperature, pressure, and permeability at depth is crucial for understanding natural-state geothermal systems. As direct observations of these quantities are limited to well locations, a reliable methodology that predicts the spatial distribution of the quantities from well observations is required. In this study, we developed a physics-informed neural network (PINN), which constrains predictions to satisfy conservation of mass and energy, for predicting spatial distributions of temperature, pressure, and permeability of natural-state hydrothermal systems. We assessed the characteristics of the proposed method by applying it to 2D synthetic models of geothermal systems. Our results showed that the PINN outperformed the conventional neural network in terms of prediction accuracy. Among the PINN-predicted quantities, the errors in the predicted temperatures in the unexplored regions were significantly reduced. Furthermore, we confirmed that the predictions decreased the loss of the conservation laws. Thus, our PINN approach guarantees physical plausibility, which has been impossible using existing machine learning approaches. As permeability investigations in geothermal wells are often limited, we also demonstrate that the resistivity model obtained using the magnetotelluric method is effective in supplementing permeability observations and improving its prediction accuracy. This study demonstrated for the first time the usefulness of the PINN to a geothermal energy problem.

1. Introduction

Modeling the temperature distribution and permeable region at depth is a fundamental procedure in geothermal development because these factors constitute a geothermal system and enable us to answer the major questions of where the heat comes from and where exploitable resources exist. The spatial extent of the permeable regions and temperature are also used for potential resource evaluation. Numerical simulations have played an important role in modeling multi-physics phenomena because heat transfer is described by partial differential equations coupling heat and fluid migration [1]. As a general development process, it is common to construct natural-state hydrothermal simulations by matching simulated and observed temperatures and pressures [3,2,4]. To construct a natural-state model, full-physics information, including the spatial distribution of physical properties and the location and quantity of the heat source that match the observations, is required. As the information at depth is mostly unknown in the geothermal field, trial-and-error and expert knowledge are mandatory. Therefore, the construction of a full-physics natural-state simulation is a very time-consuming task.

Data-driven machine learning has recently been shown to be useful for constructing subsurface models [6,5]. In particular, neural networks

(NNs) have the advantage of universal approximation and have been utilized to estimate the temperature at depth in geothermal fields [7]. In this approach, the relationship between the temperature and coordinates is trained at existing wells using an NN. The temperatures at other locations are then predicted using the trained NN. The NN approach has been applied to the Hohi geothermal region in Japan [8], the Hengill field in Iceland [9], Soultz-sous-Forêts in France [10], and the Kakkonda geothermal field in Japan [11,12]. Furthermore, porosity, which is an important property of geothermal fluid flow, has been predicted using the NN approach [13]. Despite successful applications, the major drawback of this approach is in respect to the physical evidence of the predicted quantities. Subsurface predicted quantities should follow fundamental physics laws, i.e., temperatures are distributed according to thermal conduction/convection, and thermal convection patterns are driven by fluid flow (Darcy flow), which is driven by a pressure gradient and constrained by permeability distribution.

An NN considering a certain physics law has been desired in many research fields and is considered a vital step toward the next generation of NNs. Several attempts have introduced some of the specific conditions that must be followed for the loss function of NNs [16,14,15]. Such approaches are effective under certain conditions; however, it is difficult to constrain all physical information. Raissi [17] and Raissi et al. [18] proposed the framework of a physics-informed neural network (PINN) that incorporates partial and ordinary differential equations. As fundamental physics laws, which are used in numerical simulations, are described in partial and ordinary differential forms, the PINN allows the physics laws used in numerical simulations to constrain NN predictions. Automatic differentiation (AD) plays an important role in calculating the spatial derivatives of the loss function. In contrast to numerical differentiation, AD enables the calculation of accurate derivatives without a geometric mesh. Owing to this framework, the prediction by the PINN can be regarded as a combination of data-driven and physics-driven predictions (Fig. 1). The PINN has been extended to fluid dynamics [21,19,20], computational mechanics [22,24,25,23], and material physics [26,27]. A recent review was published by Karniadakis et al. [28]. In the field of earth resources, the PINN has been used for the prediction of the hydraulic head and hydraulic conductivity in steady-state 2D (horizontal) groundwater systems using Darcy's law [30,29,31]. However, the existing PINN approach cannot be applied to geothermal systems because temperature effects and associated changes in fluid properties have not been considered. Furthermore, the benefit in one of the most important conditions in earth resource evaluation is not clear: predicting quantities in an unexplored region where wells have not been drilled.

In this study, we developed a PINN approach to predict spatial distributions of the temperature, permeability, and pressure in natural-state geothermal systems by considering the mass and energy conservation laws in the loss function. Compared with the previous studies by Tartakovsky et al. [29], He et al. [30] and Yeung et al. [31], our PINN approach accounted for temperature, resulting in multi-physics
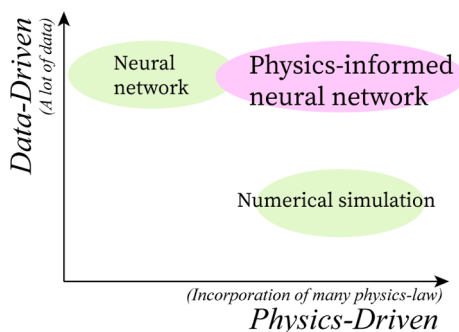
phenomena, and pore fluid properties vary according to the equation-of-state. Moreover, in contrast to these previous studies, we especially focused on assessing the prediction capability of the PINN in unexplored (extrapolation) regions as the quantities in these unexplored regions are of vital interest in geothermal development. We used 2D synthetic data to evaluate the accuracy and characteristics of the predictions using the proposed method as has been done in many previous PINN studies (e.g., [22,30,21,18,23,29]). Compared with the existing NN approach for temperature-at-depth prediction, our aim was to develop a PINN method that guaranteed that the predicted temperatures, permeabilities, and pressures followed the governing conservation equations. In addition, considering that resistivity data are often acquired in geothermal fields using the magnetotelluric (MT) method, we examined whether the resistivity obtained using the MT method can be used to decrease the prediction error of the PINN method. As the resistivity of rocks with crustal fluid is influenced by temperature, pressure, and permeability, resistivity observations have been used to estimate quantities (e.g., temperature) in geothermal fields [32,12,33] and may be useful for constraining the estimates by the PINN. We believe that our PINN method is an important milestone for developing a reliable and accurate NN for energy and earth science applications.

2. Newly developed physics-informed neural network

2.1. Governing equations of a hydrothermal system: conservation of mass and energy

The natural-state hydrothermal simulation is governed by mass and energy conservation. Mass conservation dictates that the time rate of change in the mass stored in a unit volume is equal to the net mass flux through the volume. Mass conservation implies that as crustal fluid migrates in the pores within the rock mass, the masses of crustal fluid in and out of the unit volume are identical in a steady state. In addition, equilibrium of the transported heat energy is established in a hydrothermal system. Energy conservation dictates that heat advected/conducted in should be equal to the heat advected/conducted out. Considering a steady-state and single-phase (e.g., fluid-only) condition, the mass and energy conservation equations can be described in a differential form as follows:

$$\nabla \bullet \left\{ \frac{K\rho_w}{\mu_w}(\nabla P + \rho_w g \nabla z) \right\} = 0 \ on \ V \tag{1}$$

$$\nabla \bullet \left\{ \frac{K\rho_w c_w T}{\mu_w}(\nabla P + \rho_w g \nabla z) \right\} - \nabla \bullet \lambda_r \nabla T = 0 \ on \ V \tag{2}$$

where P and T represent pressure and temperature, respectively, and K, ρ_w, μ_w, c_w, and λ_r are permeability, fluid density, fluid viscosity, fluid heat capacity, and rock thermal conductivity, respectively. g represents gravity acceleration. ∇ is a gradient vector operator indicating $\vec{i}\,\partial/\partial x + \vec{j}\,\partial/\partial y + \vec{k}\,\partial/\partial z$. The scalar product of the vector operator $\nabla \bullet \{\}$ is called divergence in vector calculus. The terms inside $\nabla \bullet \{\}$ are divided into two terms: the first term indicates mass flux driven by a pressure gradient component (∇P), and the second is driven by gravity. The energy conservation equation consists of advection and conduction terms, as heat energy is conveyed by both thermal advection and thermal conduction. The first term $\nabla \bullet \left\{ \frac{K\rho_w c_w T}{\mu_w}(\nabla P + \rho_w g \nabla z) \right\}$ in Eq. (2) indicates the influence of thermal advection, while the second term $\nabla \bullet \lambda_r \nabla T$ in Eq. (2) indicates the influence of thermal conduction. Eq. (2) assumes that the thermal energies of the crustal fluid and rock are in an equilibrium state (i.e., the temperatures of the fluid and rock are identical). As shown in Eqs. (1) and (2), temperature and pressure are coupled and nonlinearly related.

We can solve Eqs. (1) and (2) by applying the boundary conditions of temperature and pressure. The Dirichlet boundary condition imposes

Fig. 1. Schematic concept of the physics-informed neural network in comparison with a conventional neural network and numerical simulation.

constant values on surface Ξ, whereas the Neumann boundary condition imposes constant derivatives:

$$P = P_D, T = T_D \ on \ \Xi_D \tag{3}$$

$$\frac{\partial P}{\partial n} = P_N, \frac{\partial T}{\partial n} = T_N \ on \ \Xi_N \tag{4}$$

In this study, we considered K as a location-dependent variable; thus, the values are predicted by PINN, as with T and P. The other properties, including ρ_w, μ_w, and c_w are temperature- and pressure-dependent. Assuming that pure water is the crustal fluid, we implemented the model based on the formulation of IAPWS-IF95 and IAPWS-IF97 [36,34,35]. The assumption of pure water is valid when geothermal fluid is of meteoric origin.

2.2. Physics-informed loss function for a hydrothermal system

The loss function of the PINN ($LOSS$) is described as follows [32]:

$$LOSS = LOSS_m + LOSS_{phy} + LOSS_b \tag{5}$$

where $LOSS_m$ is the measure of the difference between the predictions and observations, $LOSS_{phy}$ is the constraint on partial differential equations, and $LOSS_b$ is the boundary condition. For the hydrothermal system, the physics constraint $LOSS_{phy}$ was divided into mass and energy conservation ($LOSS_{phyms}$ and $LOSS_{phyen}$). Thus, we define and minimize the following form of the loss function:

$$LOSS = LOSS_m + \kappa\left(\nu_1 LOSS_{phyms} + \nu_2 LOSS_{phyen}\right) + LOSS_{bD} + \nu_3 LOSS_{bN} \tag{6}$$

Therefore, we introduced the calibration coefficients ν_1, ν_2, and ν_3 for each physics loss with gradient operators to compensate for the difference between the loss magnitude of variables ($LOSS_m$ and $LOSS_{bD}$) and the magnitude of the loss component with derivatives ($LOSS_{phyms}$, $LOSS_{phyen}$, and $LOSS_{bN}$):

$$\nu_1 = \frac{|LOSS_m|_{epoch=0}}{|LOSS_{phyms}|_{epoch=0}}, \nu_2 = \frac{|LOSS_m|_{epoch=0}}{|LOSS_{phyen}|_{epoch=0}}, \text{and}$$

$$\nu_3 = \frac{|LOSS_m|_{epoch=0}}{|LOSS_{bN}|_{epoch=0}} \tag{12}$$

where $|LOSS_x|_{epoch=0}$ is the absolute value of $LOSS_x$ when physical constraints are imposed (the first epoch). As described in Section 2.3 in more detail, we conducted a pre-training of the PINN without constraints on physics and boundary conditions, followed by training of the PINN. Therefore, the $|LOSS_x|_{epoch=0}$ was obtained after pre-training and before the training of the PINN. The calibration coefficients ν_1, ν_2 and ν_3, were fixed during the training of the PINN.

The RMSEs of the three variables (T, P, and K) were acquired at the measurement points along the drilled wells. However, the physics constraint $LOSS_{phy}$ can be imposed on arbitrary locations within the analyzed area. The physics laws can be satisfied at the coordinates where the $LOSS_{phy}$ is imposed, while imposing the constraint at too many coordinates increases the computational load. In other words, the number of collocation points determines the fidelity of the PINN. The fidelity of the network can be tuned by controlling the number of collocation points [47].

For comparison with the PINN, we trained a conventional NN, which lacked physical information, and used the trained NN for the prediction of T, P, and K. In the following text, we refer to this setting as an NN or

$$LOSS_m = \frac{1}{N_T}\sum_{i=1}^{N_T}\left(\widehat{T_{pred,i}} - \widehat{T_{obs,i}}\right)^2 + \frac{1}{N_P}\sum_{i=1}^{N_P}\left(\widehat{P_{pred,i}} - \widehat{P_{obs,i}}\right)^2 + \frac{1}{N_K}\sum_{i=1}^{N_K}\left(log_{10}\widehat{K_{pred,i}} - log_{10}\widehat{K_{obs,i}}\right)^2 \tag{7}$$

conventional NN. The loss function of the NN is composed of $LOSS_m$ only. Therefore, the NN is purely data-driven.

2.3. PINN architecture

$$LOSS_{phyms} = \frac{1}{N_C}\sum_{i=1}^{N_C}\left(\nabla \bullet \left\{\frac{K_i\rho_{w,i}}{\mu_{w,i}}\left(\nabla P_i + \rho_{w,i}g\nabla z_i\right)\right\}\right)^2 \tag{8}$$

$$LOSS_{phyen} = \frac{1}{N_C}\sum_{i=1}^{N_C}\left(\nabla \bullet \left\{\frac{K_i\rho_{w,i}c_{w,i}T_i}{\mu_{w,i}}\left(\nabla P_i + \rho_{w,i}g\nabla z_i\right)\right\} - \nabla \bullet \lambda_r\nabla T_i\right)^2 \tag{9}$$

$$LOSS_{bD} = \sum_{i=1}^{N_{bD}}\left(\widehat{P_i} - \widehat{P_{true,i}}\right)^2 + \sum_{i=1}^{N_{bD}}\left(\widehat{T_i} - \widehat{T_{true,i}}\right)^2 \tag{10}$$

$$LOSS_{bN} = \sum_{i=1}^{N_{bN}}\left(\frac{\partial P_i}{\partial n} - P_{N,i}\right)^2 + \sum_{i=1}^{N_{bN}}\left(\frac{\partial T_i}{\partial n} - T_{N,i}\right)^2 \tag{11}$$

where $\widehat{M_{pred}}$ and $\widehat{M_{obs}}$ indicate the normalized values of the predictions and observations, respectively. N_T, N_P, and N_K are the numbers of observed T_i, P_i, and K_i, respectively. κ is a user-defined weighting coefficient that emphasizes the physical constraint on the loss function. The higher the weighting coefficient, the more strictly the physics-governing equation is satisfied. As shown in Eqs. (6)–(11), we obtained the loss functions with the variables themselves ($LOSS_m$ and $LOSS_{bD}$) using normalized values ($\widehat{T_i}$, $\widehat{P_i}$, and $\widehat{K_i}$); thus, the magnitudes of $LOSS_m$ and $LOSS_{bD}$ were compatible. On the other hand, we used absolute values (T_i, P_i, and K_i) for the losses with gradients ($LOSS_{phyms}$, $LOSS_{phyen}$, and $LOSS_{bN}$) to obtain absolute and physically meaningful quantities.

The architecture of the PINN is important for calculating accurate derivatives of the three variables (T, P, and K) with respect to the coordinates. The inputs are coordinates, and one possibility is to use a single network with multiple outputs (e.g., T, P, and K are the outputs of a single NN). However, the architecture is ineffective for calculating gradients; instead, it has been shown that a multiple network with an output of a single variable (e.g., either one of T, P, or K) leads to more accurate gradients. Therefore, in this study, we used three fully connected NNs with each variable (T, P, and K) as the output and the coordinates as the inputs (Fig. 2). Each NN was linked to the physical information and trained simultaneously (Fig. 2). The number of nodes per layer was fixed at a certain value in all layers, and the optimal number of layers and nodes/layers of the fully connected feed-forward NN used in this study was selected based on a grid search. The search candidates for the number of layers were 3, 4, and 5 for both the PINN and NN, and the number of nodes/layers was 25, 50, and 100 for the PINN and 15, 25, 50, and 100 for the NN. As the second derivative of each variable must be calculated with respect to the coordinates, the activation function should be second-order differentiable. A hyperbolic tangent was used as the activation function. For the optimizer, we implemented the adaptive moment optimization (Adam) algorithm [37]. We set the learning rate of the Adam algorithm to become progressively smaller: 5.0×10^{-5} for 0–3000 epochs, 1.0×10^{-5} for
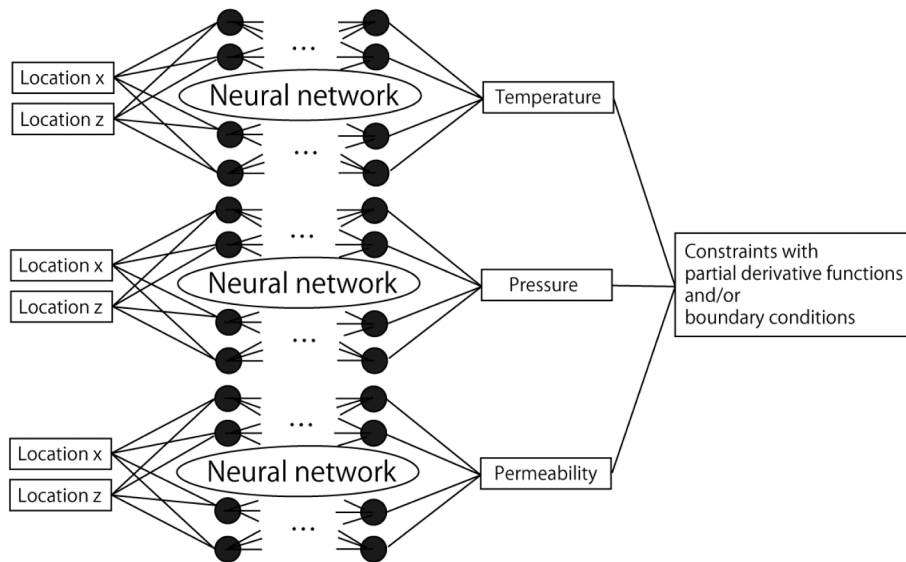
Fig. 2. Basic architecture of the physics-informed neural network (PINN) used in this study.

3001–10,000 epochs, and 5.0×10^{-6} for 10,001–final epochs. When the training of the network began, the parameters of the NNs were randomly initialized using the Xavier scheme [38]. The algorithm was implemented using TensorFlow libraries (version 2.3.1), and we used AD [39] implemented in TensorFlow to calculate the spatial derivatives of the mass and energy conservation equations.

For the convergence efficiency of the network, we first performed the training using the loss function with $LOSS_m$ for only 30,000 epochs, regardless of whether the PINN or NN was used. We subsequently

conducted an additional run for 60,000 epochs incorporating $LOSS_{phyms}$, $LOSS_{phyen}$, and $LOSS_b$ (in the case of the PINN) or using $LOSS_m$ only (in the case of the conventional NN). After the final epoch, we selected an optimal network that minimized the loss of validation data during the additional 60,000 epochs and used the optimal network for prediction. The calibration coefficients for the PINN loss function defined in Eq. (12) were obtained and fixed when the additional run of the PINN began (after 30,000 epochs of the conventional NN). Therefore, the calibration coefficients reflect the inconsistencies in the loss magnitudes between
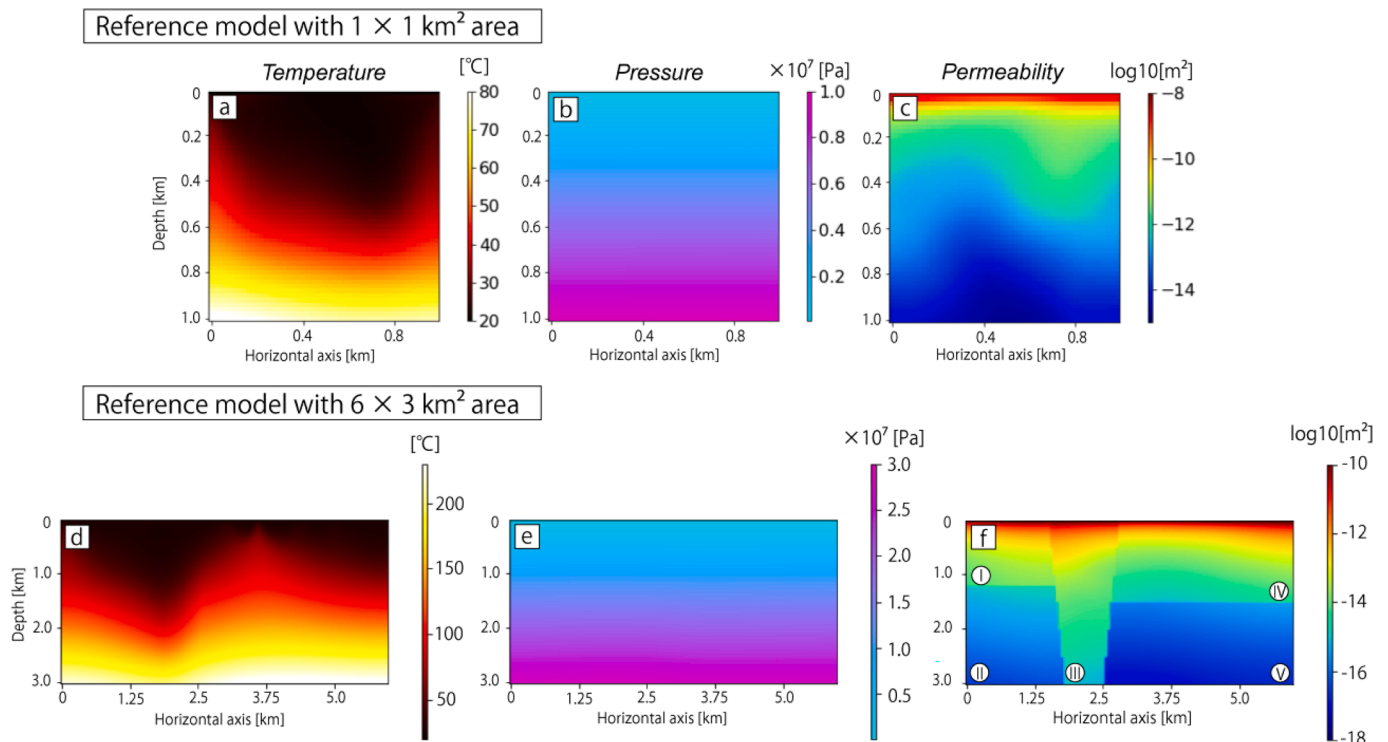

Fig. 3. Reference (a), (d) temperature T; (b), (e) pressure P; and (c), (f) permeability K used in this study. The permeability model (c) was constructed from Eqs. (13) and (14) with $\beta = 6.0$, and the block structure of (f) was created partially based on the Lahendong geothermal model [40]. The spatial distribution of permeability K was constructed from Eqs. (13) and (14) with the coefficients in Table S1. The roman numbers in (f) are the block ID in Table S1. The natural-state temperature and pressure in (a) and (b) were calculated from the permeability structure of (c), and (d) and (e) were calculated based on (f). The TOUGH2 software [41] was used for the numerical simulation.

the three variables (*T*, *P*, and *K*) and the physics or boundary constraints. The weighting coefficient κ in Eq. (6) was set as 100.

3. Synthetic data for validating the new physics-informed neural network

3.1. Simulation model setting

We considered a 2D hydrothermal system of 1 km × 1 km in the horizontal and vertical directions, with a grid size of 50 × 50 (Fig. 3a–c). Although the numerical modeling of developed commercial geothermal fields often has larger spatial scales of several kilometers, the areal size of 1 km × 1 km used in this study may be suitable when modeling less developed fields. In addition to the 1 km × 1 km model, we used a more realistic model with an area of 6 km × 3 km (Fig. 3d–f), whose permeability structure partially resembled the Lahendong geothermal field, Indonesia [40].

For the 1 km × 1 km model, the permeability of the hydrothermal system was assumed to be isotropic, and its distribution was performed by the summation of the depth-dependent and heterogenetic patterns. Depth-dependent permeability represents a regular permeability decrease due to the buried depth, and the spatial fluctuation pattern reflects the local geologic influence on permeability. For depth-dependent permeability patterns (Fig. S1a), we used the empirical equation of Manning and Ingebritsen [42]:

$$log_{10}K(z) = -alog_{10}z - b \qquad (13)$$

where $K(z)$ is the isotropic permeability in square meters (m²) and z is the depth in kilometers. The coefficients a and b were 3.2 and 14, respectively, according to Manning and Ingebritsen [42]. The empirical equation was proposed based on the isotropic and homogeneous permeability of samples collected in general geothermal environments [42].

The heterogeneity of permeability has been modeled based on the self-affinity model (e.g., [44,43]). The permeabilities were similar at short distances and became statistically different over larger distances. In this study, we simulated a heterogeneous pattern of permeability, represented by its power spectrum for the heterogenetic pattern:

$$P(\lambda) = \Lambda\lambda^{\beta} \qquad (14)$$

where $P(\lambda)$ is the power spectrum, λ is the wavenumber, and Λ and β are constants. β represents the degree of spatial correlation of the permeability; the smaller the β, the weaker the spatial correlation and the higher the heterogeneity. We considered an isotropic power spectrum of permeability for simplicity (i.e., β is identical in all directions) and used $\Lambda = 2000$ so that the magnitudes of the heterogeneous component were less than one-fourth of the regular component. For β of the 1 km × 1 km model, we used 6.0 as a base reference value (Fig. S1b), and we also used 10.0 (Fig. S1c) to understand the characteristics of the predicted values depending on the spatial complexity of the permeability distribution. The sills and ranges of the semivariogram of this permeability pattern were 0.193 log_{10}m² and 595.2 m ($\beta = 6.0$) and 0.0814 log_{10}m² and 685.4 m ($\beta = 10.0$), respectively, when the spherical model was used. The permeability distributions as the sum of the two components (regular and heterogeneous patterns) are shown in Fig. 3c and S2c for $\beta = 6.0$ and 10.0, respectively. We set the bulk thermal conductivity to 2.0 Wm⁻¹ K⁻¹ at all analyzed regions.

Assuming that the top of the simulation model corresponded to the ground surface, the upper boundary of the 1 km × 1 km synthetic data was set to a fixed temperature of 20 °C and fluid pore pressure of 1.013 × 10⁵ Pa. We assumed that the analyzed domain continued to be heated from the bottom; thus, a constant and uniform heat flux of 200 mW/m² was used as the bottom boundary. This constant heat flux is larger than the global average of crustal heat flow (50–140 mW/m²) [45,46]. However, this level is considered to be a moderate heat flux in

geothermal and volcanic areas worldwide [46,47]. No fluid and heat flow boundaries were used as the boundary side.

As a more realistic synthetic model, we created the permeability structure with 6 km and 3 km in the horizontal and vertical directions, respectively (Fig. 3f), based on the strike-slip and normal faults system of the Lahendong geothermal field [40]. In the middle of the model, we placed two faults (near-vertical block boundaries) with a dip angle of approximately 84° in the opposite direction, striking perpendicular to the model section (Fig. 3f). In the regions left and right of the faults, horizontal boundaries were placed at a depth of 1.2 km (left) and 1.5 km (right), whereas no horizontal boundary was placed between the faults (Fig. 3f). Thus, the model had five partitioned blocks (I-V in Fig. 3f). In each geological block, we considered the depth-dependent and heterogenetic patterns of permeability according to Eqs. (13) and (14). The coefficients for the depth-dependent permeability pattern *a* and *b* in Eq. (13) and those for the heterogenetic pattern Λ and β in Eq. (14) used in this model were set block-by-block and are listed in Table S1. The overall pattern of the permeability structure showed that the depth trend of permeability varied from block to block, and that permeability between the faults was higher than that of the surrounding regions (Fig. 3f). In the upper boundary, we set a fixed temperature of 25 °C and fluid pore pressure of 1.013 × 10⁵ Pa. For the bottom and side boundaries, we set the same uniform heat flux and side boundary conditions as those used in the 1 km × 1 km model. These boundary settings were different from those used in Brehme et al. [40].

3.2. Well locations

In geothermal development, direct observations of *T*, *P*, and *K* were obtained from wells drilled from the ground surface. *T* and *P* are generally observed using a thermometer and piezometer, respectively, and *K* along the wells can be observed when the rock cores are retrieved. These direct observations can be used to predict *T*, *P*, and *K* values in unexplored regions. We tested two scenarios of well placements to assess the characteristics of the PINN prediction. In the first scenario, the wells were drilled to a certain depth (vertical coordinates of 0–0.66 km in the 1 km × 1 km model and 0–2.15 km in the 6 km × 3 km model) (Fig. S3a–S3c), and *T*, *P*, and *K* were predicted using the PINN at depths where wells were not reached. In the second scenario, the wells penetrated to the bottom of the analyzed area, but at limited horizontal locations. In the second scenario, we considered the 1 km × 1 km model only, and the horizontal coordinates of the wells were set at 0–0.5 km (Fig. S3d–S3f). The second scenario was used to evaluate extrapolation performance in horizontally unexplored regions.

In the 1 km × 1 km model, we assumed that *T*, *P*, and *K* were observed at wells with a depth spacing of 20 m, and three, five, and eight wells were considered to evaluate the performance of the PINN's prediction depending on the number of wells (Fig. S3). For the 6 km × 3 km model, we considered six wells with a depth spacing of 50 m (Fig. S3g). For simplicity, the horizontal locations were uniformly spaced (Fig. S3). Of the data from the 1 km × 1 km and 6 km × 3 km models in the first scenario, we used data obtained down to 0.6 km and 2.0 km as training data, respectively, while the data within 0.6 km < depth ≦ 0.66 km (the 1 km × 1 km model) and 2.0 km < depth ≦ 2.15 km (the 6 km × 3 km model) were used as validation data to select an optimal PINN architecture. For the second scenario, the validation data were randomly selected from 20% of the total data, and the rest of the data were used as training data. The validation data were used to avoid over-fitting. Specifically, we considered the trained network that minimized the loss obtained from the validation data as the network that was not overfitted and used for prediction.

3.3. Resistivity model by MT inversion

We calculated the electrical resistivity γ for the synthetic model with 1 km × 1 km (Fig. 3a, b, and c) according to Archie's law using *T*, *P*, and

K at each model grid:

$$\gamma = \gamma_{\mathrm{w}} \phi^{-m} \tag{15}$$

where γ_{w} denotes the pore fluid resistivity. The symbols ϕ and m indicate the effective porosity and the cementation exponent, respectively. In this study, we considered a binary system of $H_2O + NaCl$ with 0.1 wt% NaCl as the pore fluid. A binary system is often used as a typical crustal fluid. The dependence of $H_2O + NaCl$ resistivity on T and P was obtained from the viscosity-dependent empirical formula developed by Watanabe et al. [48]. We calculated ϕ from K based on an empirical equation by Glover et al. [49], and the exponent m was set to 1.8, which is a representative value of porous material (i.e., rock) [50], in all analyzed regions. The resistivity of the area outside the synthetic model was set as 300 Ωm.

We synthesized the MT responses using forward modeling by solving the Maxwell equation using the controlled source audio-frequency magnetotelluric (CSAMT) method [52,51]. The CSAMT method involves transmitting a controlled electric signal at a suite of frequencies to the ground from one location and measuring the received electric and magnetic fields in the area of interest. A total of 34 CSAMT observation points were placed from −2.05–2.90 km on the horizontal coordinate (cf. the horizontal area for the PINN was 0.0–1.0 km) with a spacing of 0.15 km, and the frequency range of the impedance responses was set to 2.0–2500 Hz. The synthesized impedance responses were then transformed into apparent resistivity and phase (Fig. S4).

To invert the apparent resistivity and phase responses, we used the 2D inversion algorithms proposed by Uchida [53] and Uchida and Ogawa [54]. The inversion scheme of this algorithm minimizes both the misfit between the observed and modeled sounding curves and the smoothness of the estimated model. A smoothness parameter is introduced to control the smoothness of the estimated model, and the Akaike Bayesian information criterion (ABIC) determines the optimal smoothness parameter. The area analyzed by the CSAMT inversion was -112–113 km horizontally at 0–80 km depth, and the area was divided into 48 × 36 meshes. The horizontal and vertical mesh intervals were larger than 0.15 and 0.013 km, respectively, and were determined by the intervals of the adjacent sites. We obtained the final 2D resistivity distribution of the model in Fig. 3a, b and c after 10 iterations of the algorithm (Fig. 4). In the shallow region (<0.2 km depth), the resistivities were relatively low, but at deeper locations, the resistivities were high (Fig. 4). The apparent resistivities and phases calculated from the final resistivity distribution were in agreement with the synthetic observations (Fig. S4).
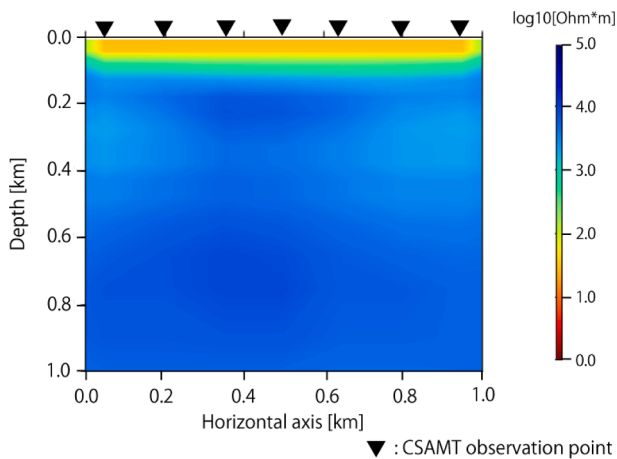
In consideration of the resistivity model in the PINN, we added the following loss function for resistivity matching to the original loss function of the PINN in Eq. (6):

$$LOSS_\gamma = \frac{1}{N_\gamma} \sum_{i=1}^{N_\gamma} \left(\gamma_{\mathrm{pred},i} - \gamma_{\mathrm{obs},i} \right)^2 \tag{16}$$

where γ_{pred} is the predicted resistivity derived from the predicted T, P, and K. When deriving γ_{pred}, we assumed that the rock-physics exponent (m in Eq. (15)) and salinity were determined from measurements prior to the PINN analysis. N_γ is the number of points used to calculate Eq. (16) from the PINN predictions and the CSAMT observations of the resistivity. The points were set to every 20 m in both the vertical and horizontal directions ($N_\gamma = 50 \times 50$).

3.4. Performance metrics

In the first scenario, which predicts quantities in the deep unexplored region, predicted T, P, and K at all simulation grids down to 0.66 km (the 1 km × 1 km model) and 2.15 km (the 3 km × 6 km model) were used to evaluate the interpolation error, while the data within 0.66–1.0 km (the 1 km × 1 km model) and 2.15–3.0 km (the 3 km × 6 km model) were used to evaluate the extrapolation error. In the second scenario, which targeted a horizontally unexplored region, the predicted values in the horizontal region of 0–0.5 km and 0.5–1.0 km were evaluated as interpolation and extrapolation errors of the 1 km × 1 km model, respectively. The prediction errors were evaluated using the following percentage error (Err (%)):

$$\mathrm{Err} = 100 \sqrt{\frac{\sum_{i=1}^{N} \left(\chi_{\mathrm{ref},i} - \chi_{\mathrm{pred},i} \right)^2}{\sum_{i=1}^{N} \chi_{\mathrm{ref},i}^2}} \tag{17}$$

where χ indicates temperature, pressure, or logarithm of permeability. The symbols χ_{ref} and χ_{pred} indicate the reference quantities of the synthetic model and the quantity predicted using the PINN (or NN), respectively. N is the number of points that measure the percentage error. For each network, architecture and synthetic data are described in Sections 2.3 and 3.1. We conducted 10 individual runs with different initial network parameters and the locations of collocation points and calculated the mean and standard deviation of the percentage error to assess the prediction performance of the proposed PINN and the conventional NN.

4. Results

4.1. Interpolation and extrapolation accuracy of the PINN in comparison with the NN

4.1.1. The first scenario (observation wells down to a certain depth)

In the first scenario of the 1 km × 1 km model (Fig. 3a–c), the loss of validation data (at the 600–660 m depth) depending on the number of layers and nodes per layer is shown in Tables S2 (PINN) and S3 (NN). Irrespective of the PINN or NN, the large number of layers and nodes tested in this study (e.g., 5 layers and 50 or 100 nodes/layer) led to a large amount of error in the validation data (e.g., loss $>10^{-4}$) (Tables S2 and S3). When the number of layers $\leqq 4$ and/or the number of nodes/layer $\leqq 50$, the validation loss was relatively small (10^{-5}–10^{-4}) (Tables S2 and S3). Of the architectures tested in this study, we used 4 layers and 50 nodes/layer and 4 layers and 25 nodes/layer for the PINN and conventional NN, respectively, as these network architectures entail a small validation error (Tables S2 and S3). The architectures were used in all the following PINN and NN-based analyses.

The predicted T, P, and K by the PINN and NN when three wells were used in the 1 km × 1 km model, together with the difference with respect

Fig. 4. Electrical resistivities of the synthetic natural-state model shown in Fig. 3a, b, and c estimated using the controlled source audio-frequency magnetotelluric (CSAMT) method. Black triangles indicate seven of the total synthetic CSAMT observation points above the horizontal range.
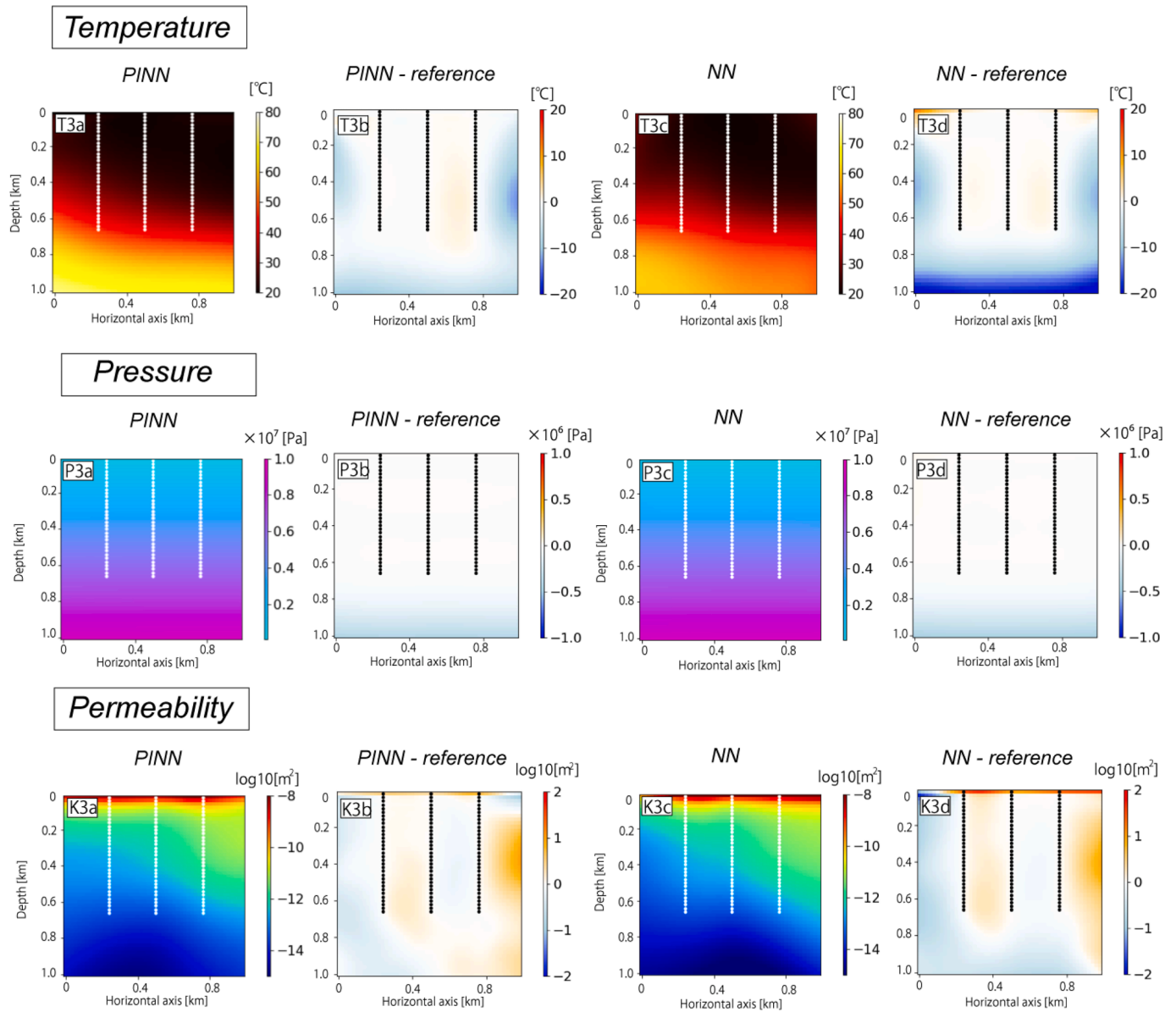
Fig. 5. Temperatures (T3a and T3c), pressures (P3a and P3c), and permeabilities (K3a and K3c) predicted using the physics-informed neural network (PINN) and neural network (NN), respectively, under the scenario 1 of the 1 km × 1 km model and three-well case. T3b, T3d, P3b, P3d, K3b and K3d show the differences between the predicted and reference values. Black and white dotted lines represent the locations of both training and validation data along the synthetic observation wells. The PINN with 4 layers and 50 nodes/layer and the NN with 4 layers and 25 nodes/layer were used for the analysis.

to the reference synthetic model, are shown in Fig. 5. All of the predicted *T*, *P*, and *K* values exhibit similar patterns to the reference model in Fig. 3a–c, showing that both the PINN and NN approaches are effective for predicting these quantities at depth. Nevertheless, the predicted *T* by the PINN was more consistent with the reference *T* compared to the predictions by the NN (T3a and T3c in Fig. 5). The *P* and *K* predicted by the PINN were similar to those predicted by the NN (P3b, P3d, K3b, and K3d in Fig. 5).

To quantitatively evaluate decreases in the prediction error, the averages and standard deviations of *T*, *P*, and *K* from the 10 individual training sessions were plotted (Fig. 6). In the case of the three wells, the average error of *T* in the interpolation depth intervals (errors from 0 to 660 m depth), returned by the PINN, was 5.9% ± 0.94% (Fig. 6a), and the average error of *T* was 8.6% ± 3.4% in the extrapolation depth intervals (errors from 660 to 1000 m depth) (Fig. 6d). These percentage errors corresponded to the absolute error of 1.9 °C ± 0.30 °C and 5.8 °C ± 2.3 °C in the interpolation and extrapolation depth intervals,

respectively. On the other hand, the average error of *T* in the interpolation and extrapolation depth intervals returned by the conventional NN were 6.5% ± 1.1% (2.1 °C ± 0.32 °C) and 10.4% ± 4.0% (6.9 °C ± 2.7 °C), respectively (Fig. 6a and d). The above results show that the predicted *T* values returned by the PINN were more accurate than those returned by the conventional NN. In particular, the PINN allowed for a more significant decrease in the prediction error at the unexplored depth (extrapolation range) compared to the prediction at the interpolation (i.e., developed) depth interval.

In the cases where the number of wells was five or eight, the prediction errors were reduced compared to the above case involving three wells (Fig. 6). This result was attributed to the larger number of wells analyzed. Graphical visualizations of the predicted *T*, *P*, and *K* values clearly show the effect of the increased number of wells had on the results (Fig. S5). Similar to the results from the three-well analysis, when five or eight wells were analyzed, the prediction accuracy of the PINN in relation to *T* was superior to that of the NN (Fig. 6a and d). Notably, *T* at
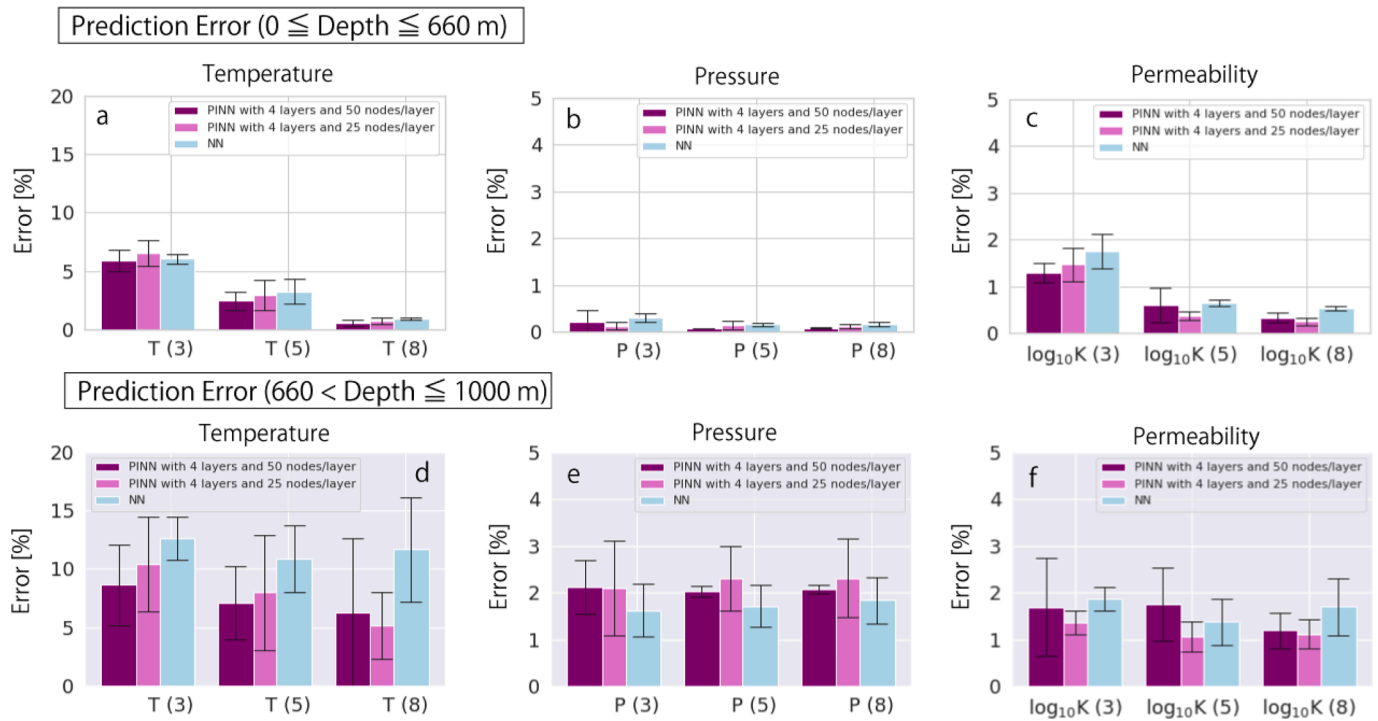
Fig. 6. (Scenario 1 and the 1 km × 1 km model) Prediction errors of the physics-informed neural network (PINN) and neural network (NN) at the interpolation and extrapolation depth ranges and with different numbers of wells. (a), (b), and (c) depict the percentage errors of temperature (*T*), pressure (*P*), and the logarithm of permeability ($\log_{10}K$) at the interpolation depth interval (0 ≦ depth ≦ 660 m), and (d), (e), and (f) depict these variables at the extrapolation depth interval (660 < depth ≦ 1000 m). The purple, light purple and light blue bars correspond to the errors returned by the PINN with 4 layers and 50 nodes/layer, PINN with 4 layers and 25 nodes/layer and NN with 4 layers and 25 nodes/layer, respectively, and the error bars represent the standard deviation from 10 individual runs. Numbers in the parentheses indicate the number of observation wells.

the depth of an unexplored (i.e., extrapolation) region decreased more significantly compared to the predictions at shallow developed (i.e., interpolation) depth intervals (Fig. 6a and d).

We found that the prediction errors for *P* and *K* returned by the PINN were almost equal to or lower than those returned by the conventional NN (Figs. 5, 6 and S5). As expected from the visual comparisons in Fig. 5, the decrease in the prediction error for *T* was more apparent than that for *P* and *K*. In other words, *T* benefited the most from the PINN approach in terms of the prediction accuracy in the unexplored region.

To verify the superior prediction accuracy of the PINN compared to the NN in another network architecture, we tested the PINN with 4 layers and 25 nodes per layer, which is the optimal architecture of the conventional NN. Light purple bars in Fig. 6 show the PINN errors, when the architecture of 4 layers and 25 nodes/layer was used, confirming that the PINN predictions were more accurate than those returned by the NN. We further confirmed the improvements in the prediction error in another synthetic model with $\beta = 10$ from Eq. (14) (Fig. S2). In this supplemental model, improvements in the prediction errors, especially in the unexplored depth interval, were also observed using the PINN (Figs. S6 and S7).

The predicted *T*, *P*, and *K* returned by the PINN and NN in the model with 6 km × 3 km area (Fig. 3d–f) are shown in Fig. 7. Similar to the predictions of the 1 km × 1 km model, the predicted *T* in the unexplored depth region was underestimated using the NN (Tc and Td in Fig. 7), whereas that returned by the PINN demonstrated a more similar pattern to that of the reference model (Ta and Tb in Fig. 7). The percentage errors of *T* at the interpolation and extrapolation depth intervals were 4.6% ± 0.7% and 4.1% ± 1.2% (PINN), and 6.0% ± 0.9% and 9.8% ± 1.3% (NN), respectively (Fig. 8a and b). The percentage errors of *T* returned by the PINN corresponded to absolute errors of 3.1 ± 0.56 °C and 9.0 ± 5.1 °C at the interpolation and extrapolation interval, respectively, and those returned by the NN were 3.27 ± 0.55 °C

(interpolation) and 17.7 ± 2.7 °C (extrapolation). Additionally, the spatial patterns of *P* and *K* predicted by the PINN were almost consistent with those of the reference model (Pa-Pd and Ka–Kd in Fig. 7). The percentage errors of the *P* and *K* returned by the PINN were almost identical or lower compared with those returned by the NN (Fig. 8a and b). Considering these results, we conclude that the PINN developed in this study outperforms an NN in prediction accuracy.

4.1.2. The second scenario (observation wells located up to a certain horizontal direction)

Fig. 9 shows examples of the predicted *T*, *P*, and *K* when the number of wells was set at three in the second scenario, with the aim of predicting the quantities in the horizontal unexplored region. The predictions from the five and eight well analyses are shown in Fig. S8. In this scenario, we also found a decrease in the prediction error using the PINN. In all well analyses, the prediction error for *T* from the unexplored region returned by the PINN was smaller than that returned by the NN (Fig. 10d). Therefore, the prediction errors for *T* from the horizontally unexplored region can also be reduced by the PINN, such as those derived during the first scenario analysis. Compared with the unexplored region, the prediction errors among the wells (interpolation region) were similar for both the PINN and NN (Fig. 10a and S8).

The prediction errors for *P* from the unexplored region were also reduced by the PINN (Figs. 9, 10b, e, and S8). The reduction in the error for *P* from the unexplored region was more significant in the second scenario than in the prediction results from the first scenario (Figs. 6e and 8e). In contrast, the prediction errors for *K* from the unexplored region returned by the PINN and NN were similar (Fig. 10f and S8). In the second scenario in relation to the interpolation region, the PINN errors for the predicted *P* were comparable to those of the NN (Fig. 10b) and the first scenario. However, the PINN errors for *K* were slightly smaller than those returned by the NN (Fig. 10c).
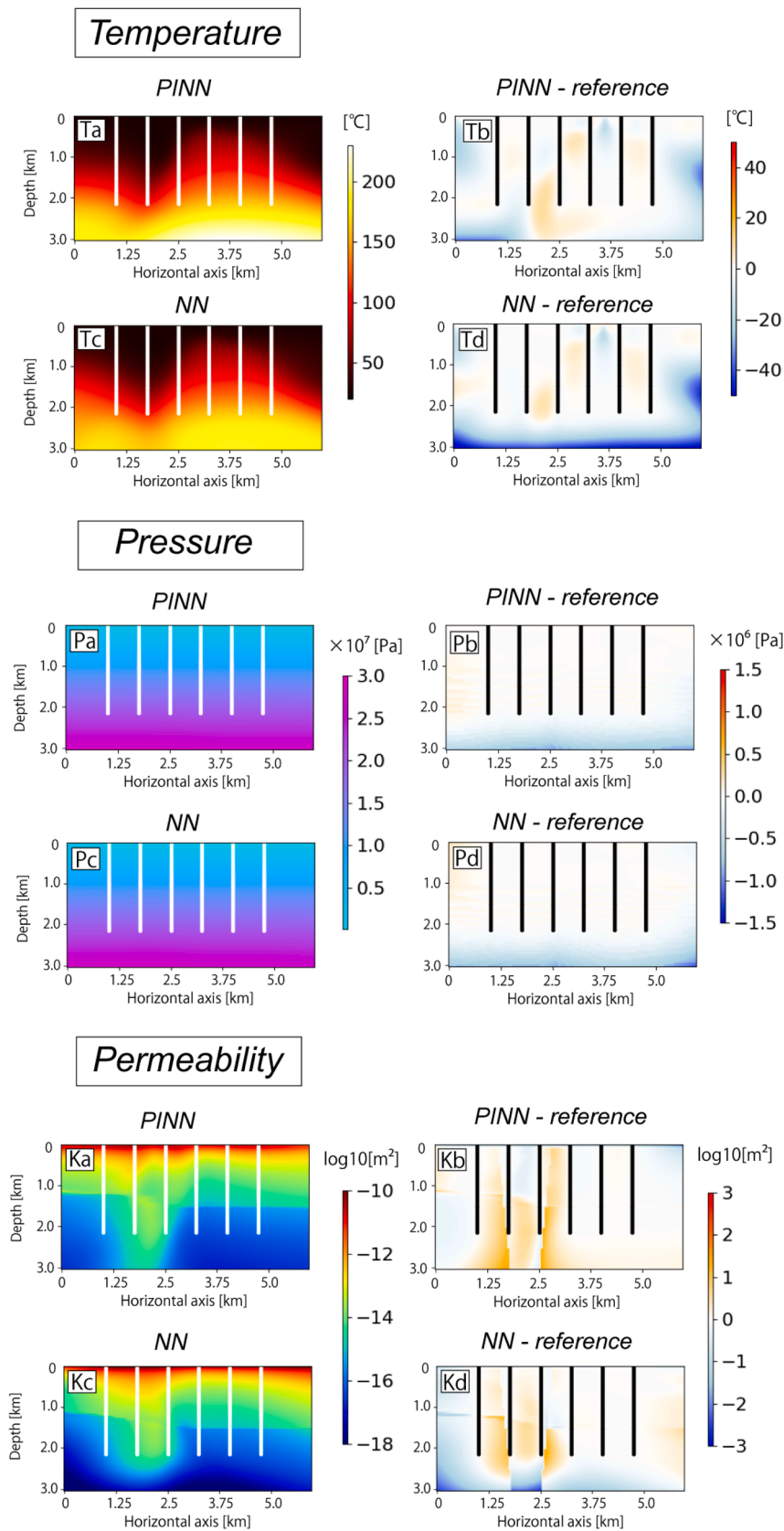
Fig. 7. Temperatures (Ta and Tc), pressures (Pa and Pc), and permeabilities (Ka and Kc) predicted using the physics-informed neural network (PINN) and neural network (NN), respectively, under scenario 1 of the 6 km × 3 km model. The PINN with 4 layers and 50 nodes/layer and the NN with 4 layers and 25 nodes/layer were used for the analysis.
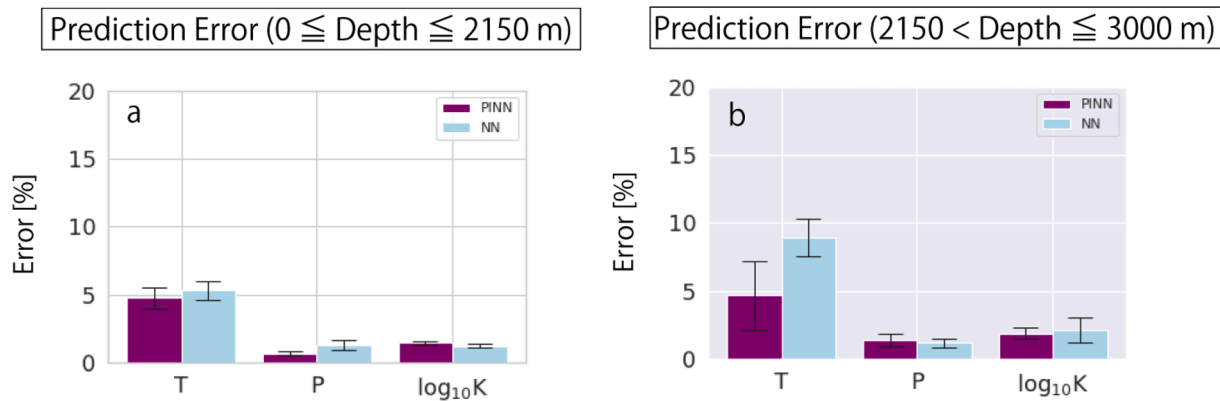
Fig. 8. (Scenario 1 and the 6 km × 3 km model) Prediction errors of the physics-informed neural network (PINN) and neural network (NN) at the (a) interpolation and (b) extrapolation depth ranges.
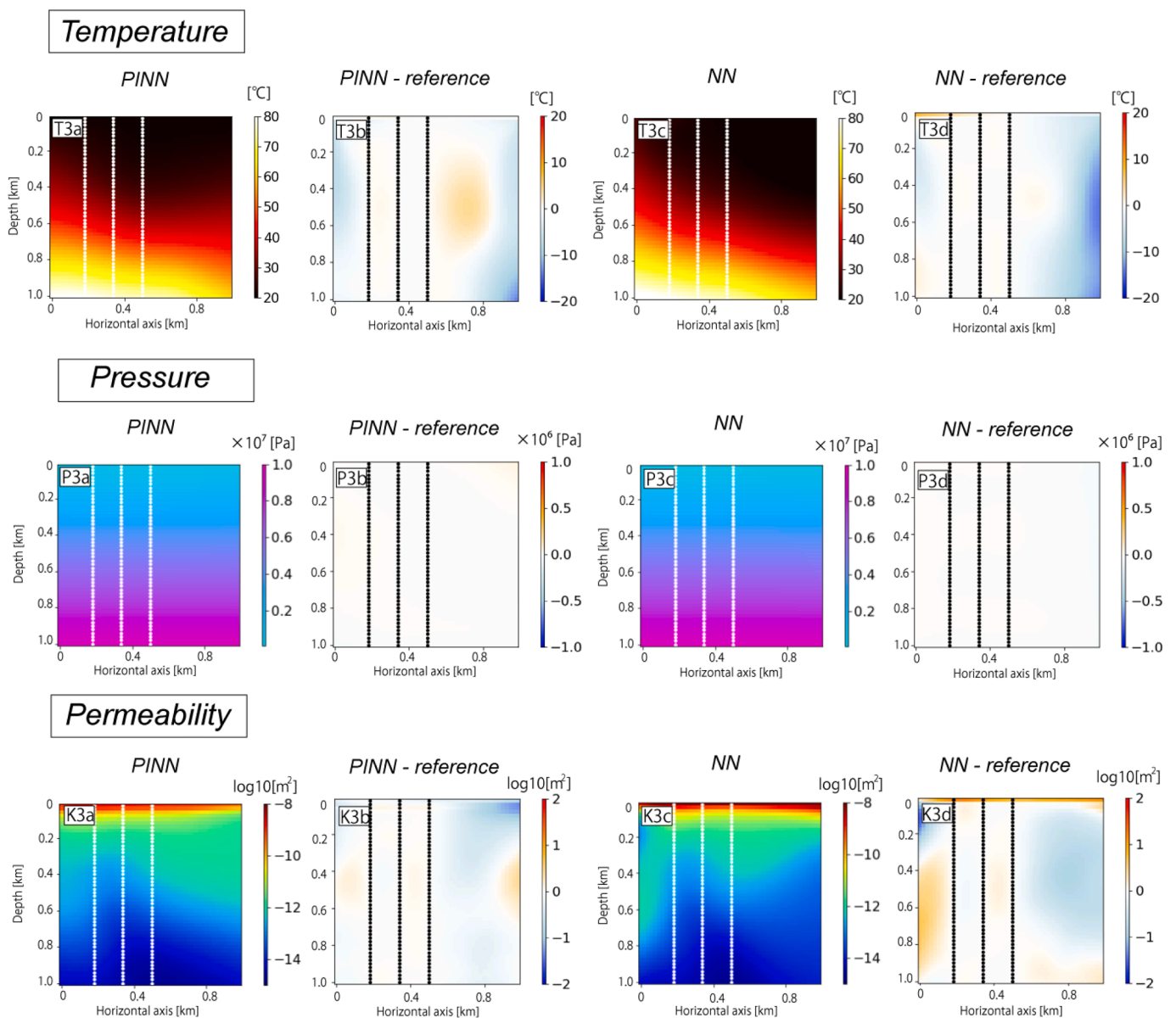

Fig. 9. The temperatures (T3a and T3c), pressures (P3a and P3c), and permeabilities (K3a and K3c) predicted using the physics-informed neural network (PINN) and neural network (NN), respectively, under the scenario 2 of the 1 km × 1 km model and the number of wells was three. T3b, T3d, P3b, P3d, K3b, and K3d are the differences between the predicted and reference values. The black and white dotted lines represent the locations of both training and validation data along the synthetic observation wells. For the analysis, the PINN with 4 layers and 50 nodes/layer and the NN with 4 layers and 25 nodes/layer were used.
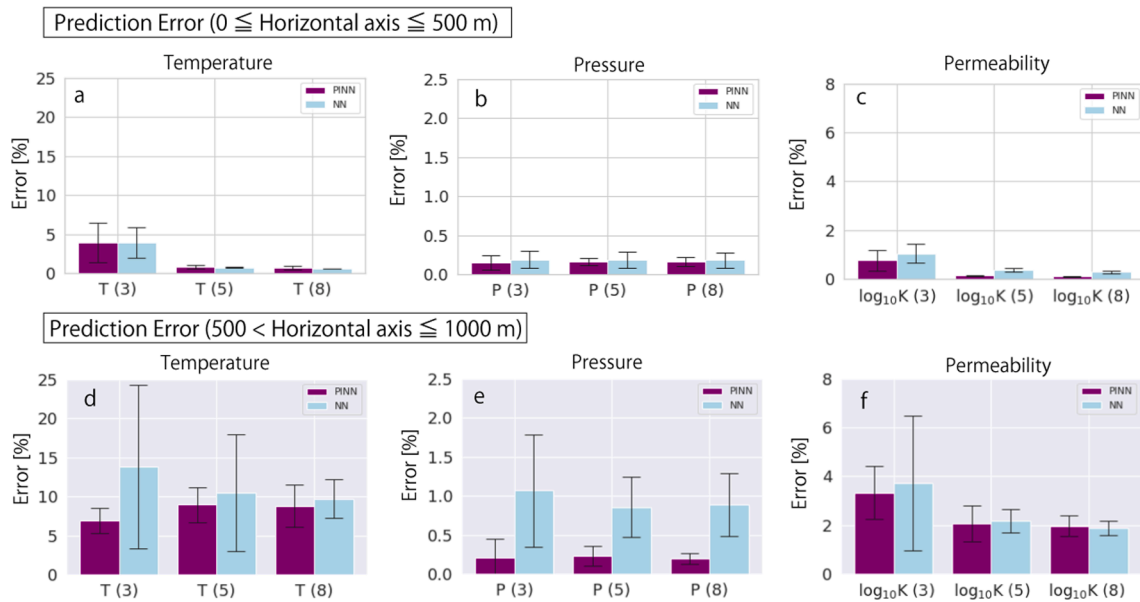
Fig. 10. (Scenario 2 and the 1 km × 1 km model) Prediction errors of the physics-informed neural network (PINN) and neural network (NN) for the interpolation and extrapolation horizontal ranges with different numbers of wells. (a), (b), and (c) depict percentage errors for temperature (*T*), pressure (*P*), and permeability (*K*) at the interpolation horizontal interval (0 ≦ horizontal axis ≦ 500 m), and (d), (e), and (f) depict these variables at the extrapolation horizontal interval (500 < horizontal axis ≦ 1000 m). The purple and light blue bars correspond to the errors returned by the PINN and NN, respectively, and the error bars represent the standard deviation from 10 individual runs. Numbers in the parentheses indicate the number of observation wells.

4.2. Conservation of mass and energy

Our results showed that the PINN predictions decreased the loss of mass and energy conservation, which was not guaranteed when using a conventional NN. Using the PINN, the average loss of the mass conservation law in Eq. (8) decreased by 4.6×10^{-2}% (three wells), 1.1×10^{-3}% (five wells), and 8.9×10^{-4}% (eight wells) compared with the same average loss when using the NN in the first scenario of the 1 km × 1 km model. In addition, the PINN decreased the average loss of the energy conservation law in Eq. (9) by 4.6×10^{-2}% (three wells), $1.1 \times$
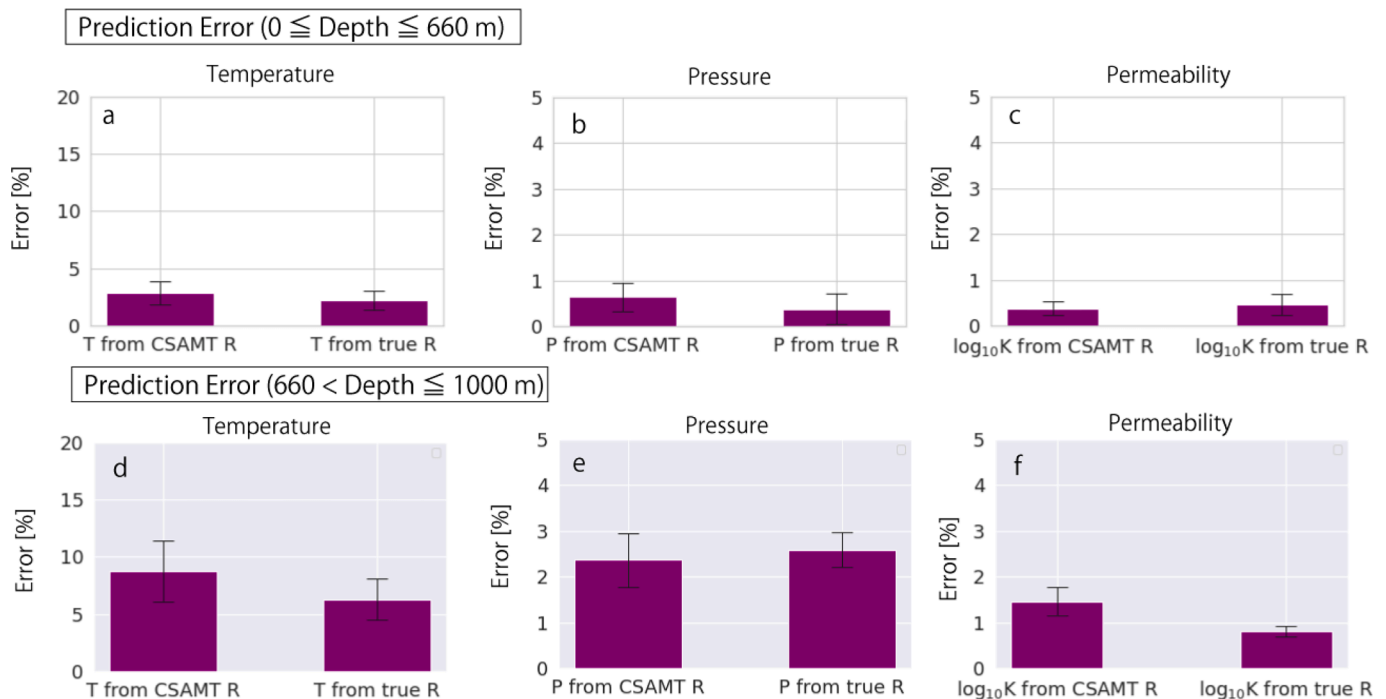

Fig. 11. (Scenario 1 and the 1 km × 1 km model) Prediction errors of the physics-informed neural network (PINN) considering the resistivity model and the five-well case. "X from CSAMT R" and "X from true R" indicate the predicted variable X (temperature (*T*), pressure (*P*) or the logarithm of permeability (*K*)) returned by the PINN incorporating the resistivity obtained by the CSAMT method and the true resistivity model (i.e., the resistivity model without the CSAMT inversion), respectively (a), (b), and (c) depict the percentage errors of temperature, pressure, and permeability at the interpolation depth interval (0 ≦ depth ≦ 660 m), and (d), (e), and (f) depict these variables at the extrapolation depth interval (660 < depth ≦ 1000 m). The error bars represent the standard deviation from 10 individual runs. The network architecture of the PINN used was 4 layers and 50 nodes/layer.

10^{-2}% (five wells), and 8.6×10^{-3}% (eight wells) compared with the same average loss when using the NN in the 1 km × 1 km model. Although the loss function and number of epochs were the same in all the well cases, the loss of conservation laws decreased with an increase in the number of wells. This result may be attributable to the fact that a larger number of wells allows the predicted values to converge more easily to the global minimum. In addition, the reduction of the losses of the conservation laws were confirmed by applying the PINN to the first scenario of the 6 km × 3 km model. The average loss of the mass and energy conservation laws in this model decreased by 4.6×10^{-3}% and 4.7×10^{-3}%, respectively.

In the second scenario, the losses of mass and energy conservation also improved when using the PINN. When using the PINN, the average loss of mass conservation reduced by 4.1×10^{-2}% (three wells), 1.9×10^{-2}% (five wells), and 2.5×10^{-1}% (eight wells) compared to the average loss of mass conservation when using the NN. The loss reduction in the conservation of energy when using the PINN was 4.1×10^{-2}% (three wells), 2.1×10^{-2}% (five wells), and 2.4×10^{-1}% (eight wells) compared to the loss reduction when using NN. Considering these results, we conclude that the T, P, and K predicted by the PINN mitigate the deviation from these conservation laws, thereby physically predicting more consistent T, P, and K values.

4.3. Use of the resistivity model by the CSAMT method

The prediction errors by accounting for the resistivity taken by the CSAMT method (shown in Fig. 4) in the scenario 1 of the 1 km × 1 km model are shown in Fig. 11. In the analysis, we considered five observation wells. Compared with the results from the PINN without considering the resistivity model (Fig. 6), the prediction errors of K at the interpolation and extrapolation depth intervals were smaller by considering the resistivity model (Figs. 6c, f, 11c and f), indicating that the resistivity model could help improve the prediction of K. When the resistivity model obtained by the CSAMT method was considered, the prediction errors for T at the extrapolation depth interval were almost same as the results from the PINN without considering the resistivity model (Figs. 6d and 11d). On the other hand, the prediction errors for T were decreased when the true resistivity model was used (Figs. 6d and 11d). The prediction errors for P at the interpolation/extrapolation depth interval slightly increased regardless of whether the CSAMT resistivity model or the true resistivity model was used (Figs. 6b, e, 11b and 11e).

We further considered a situation in which the permeabilities K could not be obtained in half of the well section. Rock core samples are commonly not retrieved from all sections along wells owing to budget limitations and/or geological conditions. When the number of wells analyzed was five and the CSAMT resistivity model was incorporated, the prediction errors for the logarithm of K were 0.51% ± 0.15% and 1.5% ± 0.15% in the interpolation and extrapolation depth intervals, respectively. On the other hand, the PINN error for K without the incorporation of the resistivity model was 0.88% ± 0.23% (interpolation) and 2.5% ± 2.5% (extrapolation). The results demonstrate that the sparsely acquired K results in the increasing error of the predicted K; however our results further showed that the error reduction for K by the resistivity model was more significant when a part of K was not acquired.

5. Discussion

5.1. Prediction error reduction in the extrapolation region by the PINN

To better understand why the predicted T in the unexplored region was greatly improved by using the PINN, we plotted the histories of each loss (Fig. 12). We found that the loss function of the training and validation data decreased and converged over epochs (Fig. 12a). Among the predicted T, P, and K values produced by the PINN, the losses of P and K
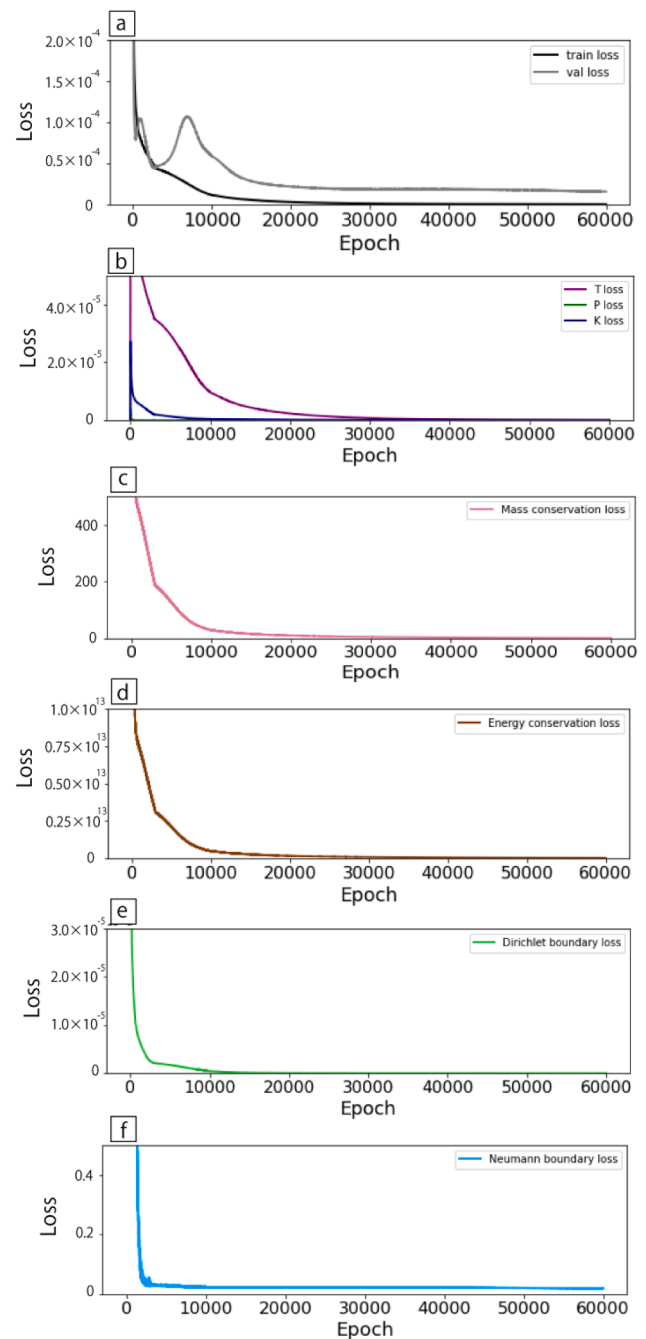

Fig. 12. Examples of the loss magnitudes of the PINN over epochs: (a) losses of training and validation data; (b) losses of temperature (T), pressure (P), and permeability (K); (c) loss of mass conservation; (d) loss of energy conservation; (e) loss of Dirichlet boundary condition; and (f) loss of Neumann boundary condition.

converged earlier than the loss of T. In addition, the convergence of the losses of mass, energy conservation, and boundary conditions was relatively slow compared to the losses of P and K, while they had almost a similar decay with the loss of T (Fig. 12b–d). These convergence patterns may indicate that T is an influential quantity in terms of the convergence of the PINN loss. This may explain why the prediction error for T decreased more significantly when using the PINN compared to the other parameters (P and K). In addition, the loss histories showed that the magnitude of losses, including derivatives (e.g., mass, energy conservation, and Neumann boundary condition), were different from the loss magnitude of the variables without derivatives (e.g., T, P, and K

alone) (Fig. 12). This difference in the loss magnitudes justifies the weighting and calibration coefficients (κ, ν_1, ν_2) introduced in Eq. (6) to compensate for the imbalance in the loss magnitude.

The prediction of the extrapolation regions produced by the NN was performed using only the observed pattern. As the observed T and K in the synthetic wells do not represent the overall pattern in the base synthetic model used, we speculated that the predictions by the NN at the extrapolation depth range were biased. In fact, even as the number of wells increased, the extrapolation error by the NN did not necessarily decrease (Fig. 6d–f). Considering these points, a conventional NN may not be able to accurately predict T, P, and K in unexplored regions based on convective temperature patterns at shallow observations, whereas the PINN approach additionally utilizes mass and energy conservation as well as boundary conditions, supporting predictions in unexplored regions. In fact, the T returned by the PINN at unexplored regions exhibit smaller error than those by the conventional NN (e.g., T3b and T3d in Fig. 5, T3b and T3d in Fig. 9). On the other hand, the conventional NN successfully predicted P at the extrapolation depth interval, as P exhibited a regular hydrostatic pattern at both the observed and non-observed locations. Nevertheless, even for the T predicted by the PINN, a small amount of error remained at locations away from the wells (e.g., T3b and T3d in Fig. 5, T3b and T3d in Fig. 9). As indicated in previous studies [12,55], this tendency for the error to increase as the distance from the well increases is a characteristic of temperature prediction using the NN-based method. Our results showed that such errors were reduced by using the PINN.

5.2. Effect of the physics constraints and boundary conditions in the PINN loss function

To investigate the influence of the losses of conservation laws (Eqs. (8) and (9)) and boundary conditions (Eqs. (10) and (11)), we conducted PINN training and prediction in the first scenario of the 1 km × 1 km model when (i) the losses of the boundary conditions were excluded from Eq. (6) (i.e., mass and energy conservations were considered in addition to the square errors of observations) and (ii) the losses of mass and energy conservations were excluded from Eq. (6) (i.e., the boundary conditions were considered in addition to the square errors of the observations). In case (i), the losses of mass and energy conservation were almost the same as those when all physics information (Eq. (6)) were considered for the loss function (Table 1). However, the errors for T were worse than those obtained when all physical information was considered (Table 1). In case (ii), the errors in T were comparable to those obtained when considering all physics and boundary conditions (Table 1). On the other hand, the predicted T, P, and K followed the mass and energy

conservation laws to a lesser extent, and the losses of the conservation laws were larger than those predicted by the NN (Table 1). Based on the above results, we conclude that the loss functions for mass and energy conservation improve predictions that satisfy these conservation laws, whereas the losses for boundary conditions improve the accuracy of predictions, especially at unexplored regions.

5.3. Spatial characteristics of the predicted permeabilities

To understand the spatial characteristics of the predicted K, we produced an empirical variogram of the predicted permeabilities. To obtain the variogram of the heterogeneous component, the regular component shown in Eq. (13), was subtracted, and the empirical variogram was derived from the remaining permeability component. The sill and range of the variogram were derived from the best-fit spherical variogram.

The semivariogram, sill and range of the predicted K produced using the PINN are in Fig. 13b–d and Table 2. Considering the sill and range of the reference permeability (Fig. 13a, Table 2), respectively, the sill and range of the predicted K were almost consistent with the reference when the number of wells was five or eight; however, the values predicted when the number of wells was three were much larger than the reference value. In other words, the spatial roughness of the reference permeability structure was accurately predicted when five and eight wells were used, whereas the spatial patterns of the predicted K from three wells were considerably smoother (did not have a fine structure) than those of the reference permeabilities. Therefore, when the number of wells was three, discrepancies were observed between the reference permeabilities and those returned by the PINN among wells (K3b in Fig. 5), whereas these discrepancies were not significant when the number of wells was five or eight (K5b and K5d Fig. S5). The discrepancies of the predicted and reference temperatures among wells when the number of wells was small (three or five) could also be caused by the spatial roughness depending on the number of wells (T3b in Fig. 5, T5b in Fig. S5).

The sill and range of the quantities predicted by the PINN were similar to those predicted by the conventional NN (Table 2). The sill and range of the predicted K values from the three wells were also considerably larger than the reference values. As the sill and range of the K predicted when using either the PINN or NN were similar, we conclude that the PINN predictions do not refine the spatial structure.

The difference in the spatial structure between the three wells and the other well numbers analyzed could be explained by the sill and range of permeabilities at the wells (Fig. 13e–g and Table 2). Owing to the sparse well locations in the case of the three wells analyzed, the sill and range were extremely high and the spatial structure of the K was not properly represented. However, the sill and range were at reasonable levels when the number of wells analyzed was five or more. From these results, we note that the spatial roughness of the predicted quantities is restricted by the number of wells and their spatial density.

Our results also suggest that the predicted distribution of K was affected by the direction of the well. The results using the model with block boundaries (the 6 km × 3 km model in Fig. 3d–f) showed that horizontal boundaries were predicted by the PINN, whereas near-vertical boundaries could not be accurately predicted. This may be because the vertical wells used in this study did not allow for dense observation of the boundary. With multiple wells inclined at an angle at which such boundaries could be observed, vertical boundaries could potentially be predicted as well.

5.4. Utility of the CSAMT resistivity model

According to our prediction results shown in Section 4.3, the incorporation of the resistivity model into the PINN approach helps decrease the prediction error for K. The resistivity model used was effective in reducing the error for K because K is one of the most influential

Table 1

Summary of the losses of the conservation laws and the error for T at the extrapolation depth interval (i) when only the conservations of mass and energy were considered and (ii) when only the boundary conditions were considered in addition to the observation mismatch. The percentage of the conservation losses was obtained with respect to the predictions by the conventional NN (see section 4.1.1).

(i) Conservations of mass and energy & observation mismatch	3 wells	5 wells	8 wells
The percentage of mass conservation loss	1.8%	1.5×10^{-2}%	1.5×10^{-2}%
The percentage of energy conservation loss	1.8%	1.5×10^{-2}%	1.5×10^{-2}%
The error of T at the extrapolation region	15.4%	13.7%	11.7%

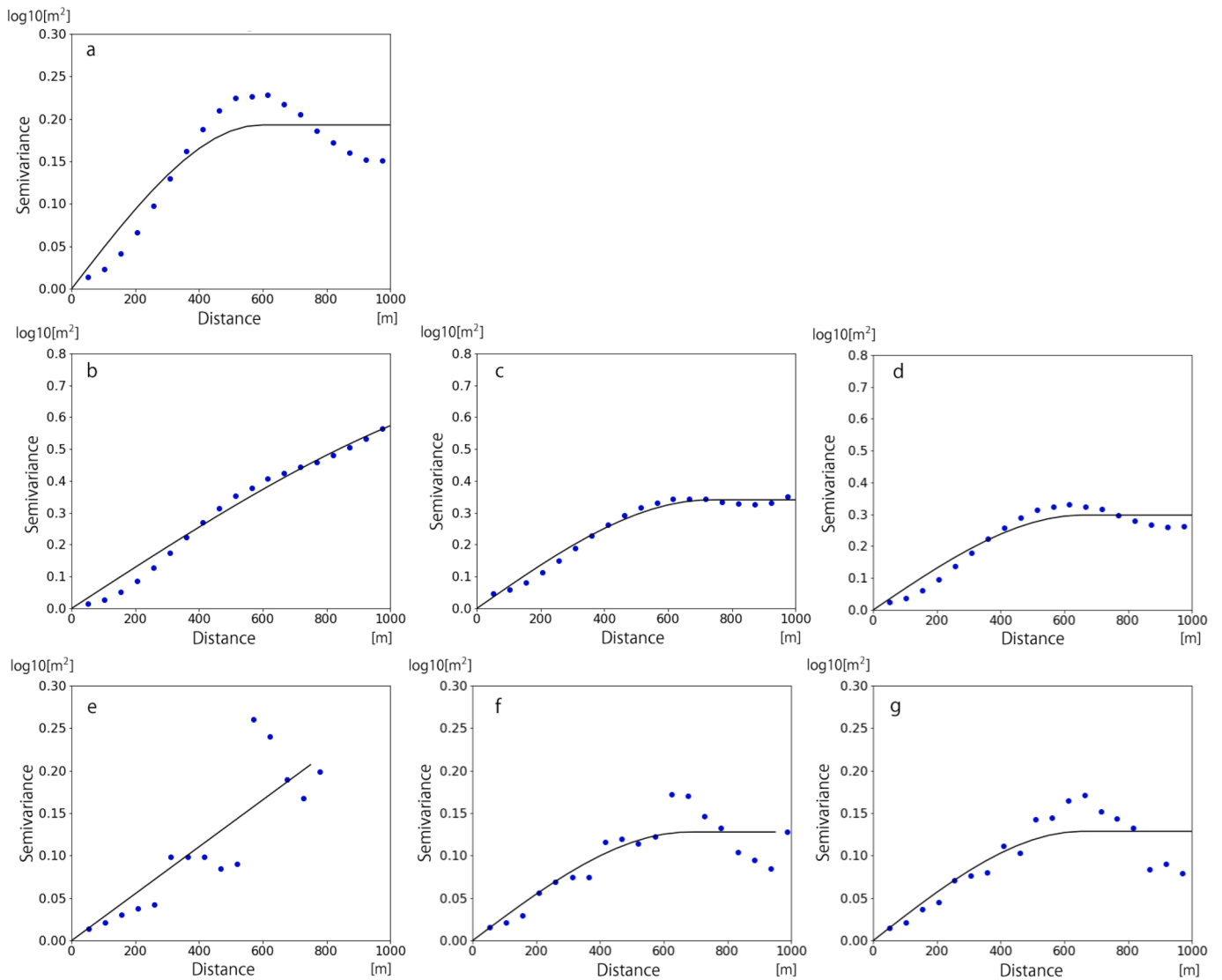| (ii) Boundary conditions & observation mismatch	3 wells	5 wells	8 wells
The percentage of mass conservation loss	392.9%	772.4%	859.6%
The percentage of energy conservation loss	390.2%	747.0%	840.8%
The error of T at the extrapolation region	8.1%	5.9%	4.8%

Fig. 13. (a) An empirical (blue dots) and best-fit theoretical (a black line) variogram of the synthetic reference permeabilities (K) (the 1 km × 1 km model with β = 6.0 in Eq. (14)). Empirical variograms of the predicted permeabilities from scenario 1, using the PINN, when the number of wells analyzed was (b) three, (c) five, and (d) eight. Empirical variograms of the permeabilities at well locations from the scenario 1 of the 1 km × 1 km model, when the number of wells analyzed was (e) three, (f) five, and (g) eight. We used a spherical model with a nugget of 0 for these theoretical variograms. (For interpretation of the references to colour in this figure legend, the reader is referred to the web version of this article.)

parameters on rock resistivity. In addition, the prediction errors for T and K were influenced by the accuracy of the resistivity model. The resistivity model obtained by the CSAMT method does not strictly reproduce the true resistivity structure owing to the ill-posed nature of the MT inversion. Therefore, when the true resistivity model (i.e., resistivities obtained directly from the synthetic model without using the CSAMT inversion) was used, the loss of T and K was much reduced. The prediction error of P was not significantly decreased even when the true resistivity model was used, likely because electrical resistivity of rock is less sensitive to pressure. Considering all the results, we conclude that an approach that incorporates the CSAMT (or MT) resistivity model in the PINN is promising as it reduces the prediction errors of T and K. As the effectiveness of the resistivity model depends on its accuracy, a refining strategy for the resistivity model may, for example, involve calibrating the resistivity model using resistivity logs and/or using newly proposed MT inversion algorithms; these are promising options. In addition to the precision of the resistivity model, we note that a proper understanding of the rock physics parameters (for example, m in Eq. (15)) is important for accurately predicting the quantities. Further, as the influence of the

resistivity model was prominent when a part of K were not acquired, we envision the usefulness of the CSAMT (or MT) resistivity model in real field applications as it can supplement sparsely acquired K observations.

6. Conclusions

Being able to predict temperature, pressure, and permeability at depth is critical to the understanding of natural-state geothermal systems. However, measurements of these variables are limited to locations in wells, beyond which the spatial distribution of these quantities is not known or easily predictable. In this study, we developed a physics-informed neural network (PINN) framework for inverse modeling of temperature, pressure, and permeability. The proposed method is data-driven in that these quantities are predicted purely by observed data. In addition to the existing data-driven approaches, we have for the first time incorporated the physics-driven approach by obeying the conservation laws of mass and energy, as well as boundary conditions.

Our validation results using 2D synthetic data of geothermal systems demonstrated that the proposed PINN reduced the prediction errors,

Table 2
The sills and ranges of the synthetic and predicted permeabilities (K) based on a best-fit theoretical variogram. The column of Figure indicates the figure numbers of the variograms corresponding to the sill and range.

	Sill [log10(m^2)]	Range [m]	Figure
Synthetic K (whole region)	0.19	595.2	Fig. 13a
Predicted K by the PINN	0.47 $\pm$ 0.28 (3 wells)	1234.4 $\pm$ 686 (3 wells)	Fig. 13b
	0.24 $\pm$ 0.043 (5 wells)	641.0 $\pm$ 45.7 (5 wells)	Fig. 13c
	0.27 $\pm$ 0.065 (8 wells)	648.6 $\pm$ 53.1 (8 wells)	Fig. 13d
Synthetic K (at wells)	>200 (3 wells)	$>10^6$ (3 wells)	Fig. 13e
	0.13 (5 wells)	679.9 (5 wells)	Fig. 13f
	0.13 (8 wells)	656.3 (8 wells)	Fig. 13g
Predicted K by the NN	0.36 $\pm$ 0.03 (3 wells)	903.7 $\pm$ 83.0 (3 wells)	
	0.23 $\pm$ 0.06 (5 wells)	586.5 $\pm$ 25.7 (5 wells)	
	0.26 $\pm$ 0.10 (8 wells)	587.7 $\pm$ 21.3 m (8 wells)	

especially in the vertically and horizontally unexplored areas, compared to the conventional neural network (NN). Furthermore, the losses of mass and energy conservation were decreased by the proposed PINN, which yields a physically more plausible prediction. The improvement in the permeability prediction by the PINN was less prominent than the temperature prediction, and further permeability along wells is sometimes difficult to acquire in geothermal fields. To overcome these limitations, we showed that the utilization of a resistivity model obtained by the magnetotellurics (MT) survey, which is generally acquired in geothermal fields, reduces the permeability prediction error. Although the effectiveness of the resistivity model depends on the accuracy of the MT inversion, recent improvements in the accuracy of the MT inversion would enhance the effectiveness of the approach.

Our results demonstrate the significant impact of the PINN approach by combining both data- and physics-driven approaches for geothermal modeling. The extension of this method to 3D modeling is straightforward. One of the limitations of the proposed method is that it does not incorporate the geological knowledge of the target site, and this will be a topic for future research. We believe that the extension of the proposed approach will be beneficial for inverse modeling in various problems in energy science and engineering.

CRediT authorship contribution statement

Kazuya Ishitsuka: Conceptualization, Data curation, Formal analysis, Funding acquisition, Investigation, Methodology, Project administration, Resources, Software, Supervision, Validation, Visualization, Writing – original draft, Writing – review & editing. **Weiren Lin:** Supervision, Writing – review & editing.

Declaration of Competing Interest

The authors declare that they have no known competing financial interests or personal relationships that could have influenced the work reported in this study.

Data availability

The synthetic data used in this study are available in the following

web site: https://doi.org/10.5281/zenodo.6818397

Appendix A. Supplementary material

Supplementary data to this article can be found online at https://doi.org/10.1016/j.apenergy.2023.120855.

References

[1] O'Sullivan MJ, O'Sullivan JP. Reservoir modeling and simulation for geothermal resource characterization and evaluation. In: DiPippo R, editor. Geothermal power generation. Woodhead Publishing; 2016. p. 165–99.

[2] O'Sullivan MJ, Pruess K, Lippmann MJ. State of the art of geothermal reservoir simulation. Geothermics 2001;30:395–429. https://doi.org/10.1016/S0375-6505(01)00005-0.

[3] Franco A, Vaccaro M. Numerical simulation of geothermal reservoirs for the sustainable design of energy plants: a review. Renew Sustain Energy Rev 2014;30: 987–1002. https://doi.org/10.1016/j.rser.2013.11.041.

[4] Ratouis TMP, O'Sullivan MJ, O'Sullivan JP. A numerical model of Rotorua geothermal field. Geothermics 2016;60:105–25. https://doi.org/10.1016/j.geothermics.2015.12.004.

[5] Yu S, Ma J. Deep learning for geophysics: current and future trends. Rev Geophys 2021;59:e2021RG000742. https://doi.org/10.1029/2021RG000742.

[6] Sun Z, Sandoval L, Crystal-Ornelas R, Mousavi SM, Wang J, Lin C, et al. A review of earth artificial intelligence. Comput Geosci 2022;159:105034. https://doi.org/10.1016/j.cageo.2022.105034.

[7] Spichak V, Zakharova OK. Electromagnetic Geothermometry. 1st ed. Elsevior; 2015.

[8] Koike K, Matsuda S, Gu B. Evaluation of interpolation accuracy of neural kriging with application to temperature-distribution analysis. Math Geol 2001;33:421–48. https://doi.org/10.1023/A:1011084812324.

[9] Spichak VV, Zakharova OK, Goidina AG. A new conceptual model of the Icelandic crust in the Hengill geothermal area based on the indirect electromagnetic geothermometry. J Volcanol Geotherm Res 2013;257:99–112. https://doi.org/10.1016/j.jvolgeores.2013.03.013.

[10] Spichak V, Geiermann J, Zakharova O, Calcagno P, Genter A, Schill E. Estimating deep temperatures in Soultz-sous-Forêts geothermal area (France) from magnetotelluric data. Near Surf Geophys 2015;13:397–408. https://doi.org/10.3997/1873-0604.2015014.

[11] Ishitsuka K, Mogi T, Sugano K, Yamaya Y, Uchida T, Kajiwara T. Resistivity-based temperature estimation of the Kakkonda geothermal field, Japan, using a neural network and neural kriging. IEEE Geosci Remote Sens Lett 2018;15:1154–8. https://doi.org/10.1109/LGRS.2018.2832647.

[12] Ishitsuka K, Kobayashi Y, Watanabe N, Yamaya Y, Bjarkason E, Suzuki A, et al. Bayesian and neural network approaches to estimate deep temperature distribution for assessing a supercritical geothermal system: evaluation using a numerical model. Nat Resour Res 2021. https://doi.org/10.1007/s11053-021-09874-w.

[13] Spichak VV, Zakharova OK. Porosity estimation at depths below the borehole from resistivity logs and electromagnetic resistivity. Near Surf Geophys 2016;14: 299–306. https://doi.org/10.3997/1873-0604.2016019.

[14] Daw A, Karpatne A, Watkins W, Read J, Kumar V. Physics-guided neural networks (PGNN): an application in lake temperature modeling. arXiv:1710.11431. 2017. https://doi.org/10.48550/arXiv.1710.11431.

[15] Jia X, Willard J, Karpatne A, Read J, Zwart J, Steinbach M, et al. Physics guided RNNs for modeling dynamical systems: A case study in simulating lake temperature profiles. In: Proceedings of the 2019 SIAM international conference on data mining (SDM); 2019. p. 558–66. https://doi.org/10.1137/1.9781611975673.63.

[16] Chen Y, Zhang D. Physics-constrained deep learning of geomechanical logs. IEEE Trans Geosci Remote Sens 2020;58:5932–43. https://doi.org/10.1109/TGRS.2020.2973171.

[17] Raissi M. Deep hidden physics models: deep learning of nonlinear partial differential equations. J Mach Learn Res 2018;19:1–24.

[18] Raissi M, Perdikaris P, Karniadakis GE. Physics-informed neural networks: a deep learning framework for solving forward and inverse problems involving nonlinear partial differential equations. J Comput Phys 2019;378:686–707. https://doi.org/10.1016/j.jcp.2018.10.045.

[19] Mao Z, Jagtap AD, Karniadakis GE. Physics-informed neural networks for high-speed flows. Comput Methods Appl Mech Eng 2020;360:112789. https://doi.org/10.1016/j.cma.2019.112789.

[20] Sun L, Gao H, Pan S, Wang JX. Surrogate modeling for fluid flows based on physics-constrained deep learning without simulation data. Comput Methods Appl Mech Eng 2020;361:112732. https://doi.org/10.1016/j.cma.2019.112732.

[21] Jin X, Cai S, Li H, Karniadakis GE. NSFnets (Navier-stokes floe nets): physics-informed neural networks for the incompressible Navier-stokes equations. J Comput Phys 2021;426:109951. https://doi.org/10.1016/j.jcp.2020.109951.

[22] Goswami S, Anitrscu C, Chakraborty S, Rabczuk T. Transfer learning enhanced physics informed neural network for phase-field modeling of fracture. Theor Appl Fract Mech 2020;106:02447. https://doi.org/10.1016/j.tafmec.2019.102447.

[23] Samaniego E, Anitescu C, Goswami S, Nguyen-Thanh VM, Guo H, Hamdia K, et al. An energy approach to the solution of partial differential equations in computational mechanics via machine learning: concepts, implementation and applications. Comput Methods Appl Mech Eng 2020;362:112790. https://doi.org/10.1016/j.cma.2019.112790.

[24] Haghighat E, Raissi M, Moure A, Gomez H, Juanes R. A physics-informed deep learning framework for inversion and surrogate modeling in solid mechanics. Comput Methods Appl Mech Eng 2021;379:113741. https://doi.org/10.1016/j.cma.2021.113741.

[25] Rao CP, Sun H, Liu Y. Physics-informed deep learning for computational elastodynamics without labeled data. J Eng Mech 2021;147:04021043. https://doi.org/10.1061/(ASCE)EM.1943-7889.0001947.

[26] He Z, Ni F, Wang W, Zhang J. A physics-informed deep learning method for solving direct and inverse heat conduction problems of materials. Mater Today Commun 2021;29:102719. https://doi.org/10.1016/j.mtcomm.2021.102719.

[27] Shen S, Lu H, Sadoughi M, Hu C, Nemani V, Thelen A, et al. A physics-informed deep learning for bearing fault detection. Eng Appl Artif Intel 2021;103:104295. doi: j.engappai.2021.10495.

[28] Karniadakis GE, Kevkidis IG, Lu L, Perdikaris P, Wang S, Yang L. Physics-informed machine learning. Nat Rev Phys 2021;3:22–440. https://doi.org/10.1038/s42254-021-003145.

[29] Tartakovsky AM, Marrero CO, Perdikaris P, Tatakovsky GD, Barajas-Solano D. Physics-informed deep neural networks for learning parameters and constitutive relationships in subsurface flow problems. Water Resour Res 2020;56: e2019WR026731. https://doi.org/10.1029/2019WR026731.

[30] He Q, Barajas-Solano D, Tartakovsky G, Tartakovsky AM. Physics-informed neural networks for multiphysics data assimilation with application to subsurface transport. Adv Water Resour 2020;14:103610. https://doi.org/10.1016/j.advwatres2020.103610.

[31] Yeung YH, Barajas-Solano DA, Tartakovsky AM. Physics-informed machine learning method for large-scale data assimilation problems. Water Resour Res 2022;58:e2021WR031023. https://doi.org/10.1029/2021WR031023.

[32] Hokstad K, Tänavsuu-Milkeviciene K. Temperature prediction by multigeophysical inversion: Application to the IDDP-2 well at Reykjanes, Iceland. GRC Trans 2017: 41.

[33] Ishitsuka K, Yamaya Y, Watanabe N, Kobayashi Y, Mogi T, Asanuma H, et al. Constraining temperature at depth of the Kakkonda geothermal field, Japan, using Bayesian rock-physics modelling of resistivity: implications to the deep hydrothermal system. Geothermics 2022;100:102316. https://doi.org/10.1016/j.geothermics.2021.102316.

[34] Wagner W, Cooper JR, Dittmann A, Kijima J, Kretzschmar HJ, Kruse A, et al. The IAPWS industrial formulation 1997 for the thermodynamic properties of water and steam. Trans ASME 2000;122:150–82.

[35] Wagner W, Pruβ A. The IAPWS formulation 1995 for the thermodynamic properties of ordinary water substance for general and scientific use. J Phys Chem Ref Data Monogr 2002;31:387. https://doi.org/10.1063/1.1461829.

[36] Huber ML, Perkins RA, Laesecke A, Friend DG, Sengers JV, Assael MJ, et al. New international formulation for the viscosity of H_2O. J Phys Chem Ref Data Monogr 2009;38:101. https://doi.org/10.1063/1.3088050.

[37] Kingma D, Ba J. Adam: a method for stochastic optimization. arXiv 2014. https://doi.org/10.48550/arXiv.1412.6980. preprint, arXiv:1412.6980.

[38] Glorot X, Bengio Y. Understanding the difficulty of training deep feedforward neural networks. In: Proceedings of the Thirteenth International Conference on Artificial Intelligence and Statistics; 2010. p. 249–56.

[39] Baydin AG, Pearlmutter BA, Radul AA, Siskind JM. Automatic differentiation in machine learning: a survey. J Mach Learn Res 2018;18:1–43.

[40] Brehme M, Blocher G, Cacace M, Kamah Y, Sauter M, Zimmermann G. Permeability distribution in the Lahendong geothermal field: a blind fault captured by thermal-hydraulic simulation. Environ Earth Sci 2016;75:1088. https://doi.org/10.1007/s1265-016-5878-9.

[41] Pruess K. The TOUGH2 codes – a family of simulation tools for multiphase flow and transport in permeable media. Vadose Zone J 2004;3:738–46. https://doi.org/10.2136/vzj2004.0738.

[42] Manning CE, Ingebritsen SE. Permeability of the continental crust: implications of geothermal data and metamorphic systems. Rev Geophys 1999;37. https://doi.org/10.1029/1998RG900002. 1998RG900002.

[43] Watanabe N, Wang W, McDermott CI, Taniguchi T, Kolditz O. Uncertainty analysis of thermo-hydro-mechanical coupled processes in heterogeneous porous media. Comp Mech 2009;45:263. https://doi.org/10.1007/s00466-009-0445-9.

[44] Niederau J, Ebigbo A, Marquart G, Arnold J, Clauser C. On the impact of spatially heterogeneous permeability on free convection in the Perth Basin. Australia Geotherm 2017;66:119–33. https://doi.org/10.1016/j.geothermics.2016.11.011.

[45] Beardsmore GR, Cull JP. Curstal heat flow - a guide to measurement and modelling, chapter 1. Cambridge University Press; 2001.

[46] Davis JH. Global map of solid earth surface heat flow. Geochem Geophys Geosyst 2013;14:4608–22. https://doi.org/10.1002/ggge.20271.

[47] Kissling WM, Weir GJ. The spatial distribution of the geothermal fields in the Taupo volcanic zone, New Zealand. J Volcanol Geotherm Res 2005;145:136–50. https://doi.org/10.1016/j.volgeores.2005.01.006.

[48] Watanabe N, Yamaya Y, Kitamura K, Mogi T. Viscosity-dependent empirical formula for electrical conductivity of H_2O-NaCl fluids at elevated temperatures and high salinity. Fluid Phase Equilibria 2021;549:113187. https://doi.org/10.1016/j.fluid.2021.113187.

[49] Glover PWJ, Zadjali II, Frew KA. Permeability prediction from MICP and NMR data using an electrokinetic approach. Geophysics 2006;71:F40–60. https://doi.org/10.1190/1.2216930.

[50] Glover PWJ. Geophysical properties of the near surface earth: electrical properties. In: Treatise on geophysics; 2015. p. 89–137. https://doi.org/10.1016/B978-0-444-53802-4.0089-5.

[51] Sasaki Y, Yoneda Y, Matsuo K. Resistivity imaging of controlled-source audiofrequency magnetotelluric data. Geophysics 1992;57:855–952. https://doi.org/10.1190/1.1443309.

[52] Routh PS, Oldenburg DW. Inversion of controlled source audio-frequency magnetotellurics data for a horizontally layered earth. Geophysics 1999;64: 1689–97. https://doi.org/10.1190/1.1444673.

[53] Uchida T. Smooth 2-D inversion for magnetotelluric data based on statistical criterion ABIC. J Geomag Geoelec 1993;45:841–58.

[54] Uchida T, Ogawa Y. Development of Fortran code for two-dimensional magnetotelluric inversion with smoothness constraint. Geol Surv Japan Open-File Rep 1993;205:115.

[55] Spichak VV, Zakharova OK, Rybin AK. Methodology of the indirect temperature estimation basing on magnetotelluric data: northern Tien Shan case study. J Appl Geophys 2011;73:164–73. https://doi.org/10.1016/j.jappgeo.2010.12.007.